Journal of Power Sources 196 (2011) 7721–7727

Contents lists available at ScienceDirect

Journal of Power Sources

journal homepage: www.elsevier.com/locate/jpowsour

# Degradation analysis of a Ni-based layered positive-electrode active material cycled at elevated temperatures studied by scanning transmission electron microscopy and electron energy-loss spectroscopy

Y. Kojima [a], S. Muto [a,*], K. Tatsumi [a], H. Kondo [b], H. Oka [b], K. Horibuchi [b], Y. Ukyo [b]

[a] Graduate School of Engineering, Nagoya University, Chikusa-ku, Nagoya 464-8603, Japan
[b] Toyota Central R&D Laboratories Inc., Nagakute 480-1192, Japan

ARTICLE INFO

*Article history:*
Received 25 November 2010
Received in revised form 25 April 2011
Accepted 11 May 2011
Available online 19 May 2011

*Keywords:*
Lithium ion secondary battery
Cathode
Capacity fading
Scanning transmission electron microscopy
Electron energy-loss spectroscopy

ABSTRACT

We investigate the local structural changes in a positive electrode of a lithium ion secondary battery ($LiNi_{0.8}Co_{0.15}Al_{0.05}O_2$ (NCA) as the active material) associated with charge–discharge cycling at elevated temperatures by scanning transmission electron microscopy (STEM) and electron energy-loss spectroscopy (EELS). STEM–EELS spectral imaging reveals the evolution of a NiO-like phase localized near the surface and grain boundary regions after many cycles. The amounts of capacity fading and resistance increase are discussed based on the results of the semiquantitative estimation of NiO-like and other product phases. We also identify the chemical state of lithium in the NiO-like phase substituting for Ni.


## 1. Introduction

Rechargeable lithium ion batteries are now widely used in portable equipment because of their high energy densities and voltages. Their applications are expected to be extended to power supplies for electric vehicles (EVs), hybrid electric vehicles (HEVs) and plug-in HEVs (PHEVs). To improve battery performance for such practical applications, it is necessary to develop basic technologies including research and development of better cathode and anode materials, and electrolytes. Balanced cell performance is also necessary in terms of safety, lifetime, cost, power and energy density. In particular, considering the automotive applications of lithium ion batteries, it is imperative to develop alternative cathode materials to $LiCoO_2$ from the viewpoint of cost and depletion of resources. Layered $LiNiO_2$ [1,2] and its related materials [3–9] are attractive materials because of their relatively less serious problems in terms of resources, their high capacity and high rate performance. However, $LiNiO_2$-based materials exhibit significant degradation such as capacity fading and impedance rise when used at elevated temperatures [10–19]. According to the degradation analysis of batteries using $LiNi_{0.8}Co_{0.2}O_2$ [10–14] and Al/Co co-doped $LiNiO_2$-based cathode materials [15–19], the impedance rise of the positive electrode is mainly responsible for the degradation of the entire cell [10,11,16–19]. To elucidate the degradation mechanism under high-temperature operations, cathode materials have been analyzed by some research groups using macroscopic methods such as electrochemical measurements [10,11,16–19], X-ray photoelectron spectroscopy (XPS) [13], X-ray diffraction analysis [15,16] and X-ray absorption fine structure (XAFS) analysis [12,14,18,19]. Among the various degradation mechanisms proposed, the degradation of $LiNiO_2$-based cathode materials through the irreversible formation of inactive divalent or trivalent Ni species, particularly those localized in surface regions, has been shown by our group [19] and another group to be the most viable mechanism [12,14]. However, since the material degradation associated with electrochemical or chemical reactions should start somewhere at nanometer-scale areas in the entire positive electrode extending over a few tens of micrometers from the surface to the electron collector, it is crucial to examine wider areas of the electrode with high spatial resolution, linking the gap between the macroscopic electrochemical measurements and microscopic structural changes, that is, identifying when, where and how the degradation starts and progresses. Microscopic methods such as high-resolution (scanning) transmission electron microscopy (HR(S)TEM) and nano-electron diffraction (nano-ED) analysis require good sample crystallinity and proper alignment to the correct crystal orientation to obtain informative data, and this may not be always possible, particularly in materials for practical use, and more so in materials where degradations

* Corresponding author. Tel.: +81 52 789 5200; fax: +81 52 789 4684.
*E-mail address:* s-mutoh@nucl.nagoya-u.ac.jp (S. Muto).

0378-7753/$ – see front matter © 2011 Elsevier B.V. All rights reserved.
doi:10.1016/j.jpowsour.2011.05.017

occur. Furthermore, one can select a local observation result that agrees well with macroscopic measurements, although such an observation is not always representative of the entire microstructure.

Electron energy-loss spectroscopy (EELS) combined with STEM, particularly core state excitation spectral (energy-loss near edge structure: ELNES) analysis, conveys information on local chemical environments, or local atomic configurations around specific elements [20]. ELNES projects the three-dimensional local structure onto a one-dimensional energy-loss axis, which is generally independent of crystal orientation. STEM–EELS is thus an ideal tool for the problem at hand because local structural changes associated with material degradation can be visualized simply by scanning the nanosized electron probe on wide areas of the sample of interest and analyzing the data obtained with a statistical method, called multivariate curve resolution (MCR).

By applying the method mentioned above, we have observed in a $LiNi_{0.8}Co_{0.15}Al_{0.05}O_2$ (NCA) cathode sample a NiO-like phase (containing divalent Ni) with the rock-salt structure near the surface and grain boundary regions of active material particles both before and after a cycling test performed at 80 °C, and substantial phase evolution (thickening) was found after the cycling [20]. We have also found that the spatial distribution of the NiO-like phase highly correlates with the fluorine distribution, indicating that the degradation of the cathode takes place by surface reactions between active materials and the electrolyte [20]. We called the product phase the 'NiO-like' phase, which refers to the local atomic configuration and chemical states probed by EELS rather than to a long-range order having translational symmetry.

Since our analysis method works well for samples cycled at 80 °C that are heavily degraded, we consider it interesting to examine similar samples cycled at practically more realistic temperatures. In the present study, the same methodology used in our previous studies [21,22] is applied to the examination of an NCA-positive electrode cycled at 70 °C, which exhibits moderate degradation, and capacity fading and resistance increase observed by macroscopic electrochemical measurements are discussed, and quantitatively compared with microscopic information.

## 2. Experimental and analysis methods

### 2.1. Cell preparation and cycling test

Charge–discharge cycling tests at elevated temperatures (70 and 80 °C) were performed on 500 mAh-type cylindrical cells with $LiNi_{0.8}Co_{0.15}Al_{0.05}O_2$ and graphite as the positive and negative electrode materials, respectively. The detailed cell fabrication has already been described elsewhere [19]. A polyethylene separator was wound around the positive and negative electrodes, which were then put into a cylindrical cell case with 1 mol $l^{-1}$ $LiPF_6$ dissolved in an ethylene carbonate/dimethyl carbonate/ethylmethyl carbonate (EC/DMC/EMC) mixed solvent (3:4:3 by volume). Cycling tests were carried out at rate of 2 C for 500 cycles in the range of 3.0–4.1 V at 70 and 80 °C after a few initial conditioning charge–discharge cycles. We already confirmed that the degree of degradation is the same for the calendar-life test for 7 months and the present cycling test, and the degradation mechanism is almost the same for the two.

### 2.2. Electrochemical evaluation of positive electrode

After the cycling tests, the cycled cell was disassembled in an Ar-filled glovebox. The cell subjected to only the initial conditioning cycles was also disassembled in the same manner for comparison. The collected positive electrodes were rinsed with dimethyl carbonate three times to completely remove the residual electrolyte before the electrochemical measurements and spectroscopic analysis using TEM.

To estimate the degree of capacity fading, electrochemical measurements were carried out using three electrode cells with lithium metal as the counter and reference electrodes. The charge–discharge profiles of the positive electrodes from the fresh and cycled cells were recorded in the potential range between 3.0 and 4.1 V vs. $Li^+/Li$ with a constant current rate of 0.1 C per cycle. Cyclic voltammetry was also performed in the potential range between 3.0 and 4.5 V vs. $Li^+/Li$ with a scan rate of 0.2 mV $s^{-1}$ at 20 °C.

### 2.3. Spectral imaging and MCR processing

The collected positive electrodes were electrochemically discharged to 3.0 V vs. $Li^+/Li$ and then set to the constant voltage of 3.0 V vs. $Li^+/Li$ for 5 h before the STEM–EELS analysis. A focused ion beam thinning technique was used to prepare uniform thin films (~100 nm thick) of the obtained positive electrodes over an area as large as ~10 μm for STEM–EELS. SI data were acquired at room temperature using a Jeol JEM2100 S/TEM system for the low-loss region (including Li–K, Co- and Ni-$M_{2,3}$ absorption edges) and a JEM2100F S/TEM system for the high-energy region (including O–K, Co-$L_{2,3}$ and Ni-$L_{2,3}$ edges), both equipped with a Gatan Enfina 1000 spectrometer, using a probe size of 6 nm, an acquisition time of 0.8 s and a scan step of 10 nm in the former and a probe size of 0.3 nm, an acquisition time of 0.5 s and a scan step of 10 nm in the latter. The energy dispersion was set to 0.1 eV $channel^{-1}$ with an energy loss range from −10 to 120 eV including the zero loss peak (ZLP) in the former and to 0.3 eV $channel^{-1}$ with an energy loss range from 500 to 900 eV in the latter. The spectral drift correction, pre-edge background subtraction and deconvolution to remove the plural scattering were performed similarly to those in previous studies [19,20]. The carbon binder region surrounding the active material particles was carefully excluded for the MCR analysis of the higher-energy-loss region because the O K ELNES in the binder region exhibited a profile very similar to the degraded phase of the active material, which can cause additional errors in the analysis.

As reported previously [21,22], the MCR technique is beset with two inherent difficulties: one is that the number of components underlying cannot be determined a priori; the other is that the result obtained by means of the MCR technique is not unique. In general, the number of components is increased one by one until the spatial distribution of the residual seems to be random statistical noise with no spatial structure. To check out the uniqueness and validity of the spectral decomposition we also confirmed whether identical spectral profiles of the resolved components with very similar spatial distributions are obtained by independently applying the MCR to a number of secondary particles.

### 2.4. Theoretical prediction of Li K ELNES

We calculated theoretical ELNES for possible compounds using the augmented plane wave plus local orbital (APW + lo) band method within the generalized gradient approximation (GGA; using the WIEN2k code) [23,24] to compare the relative peak intensities and positions of the experimental and theoretical spectra. For Ni *d* states, we adopted the same Hubbard-type orbital-dependent interaction, as described previously [23]. The $3 \times 3 \times 3$ supercell of the primitive cell containing 128 atoms per supercell with a core hole introduced at the excited atom was used. Prior to the spectral calculations, the structural parameters were optimized using the projected augmented wave method (VASP code). The atom positions were freely relaxed under the constraint of the given

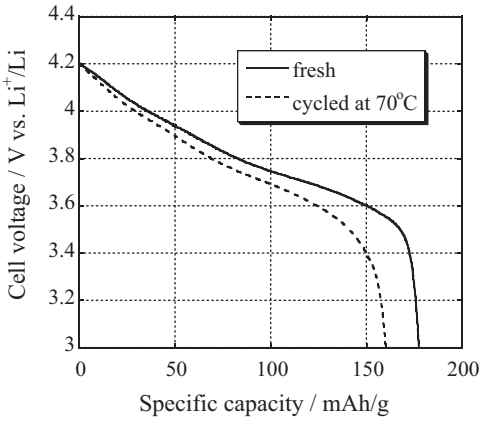


**Fig. 1.** Discharge curves of positive electrodes obtained from fresh and cycled batteries at 70 °C.

symmetry of the supercell within the fixed supercell size until the residual force was reduced to less than 0.05 eV Å$^{-1}$. The final ELNES spectrum was broadened using a Gaussian function with an FWHM (full-width at half-maximum) of 1.0 eV. The energy loss axis was calibrated using the experimental and theoretical spectra of the known standards of $Li_2O$ and $LiNiO_2$.

## 3. Results and discussion

### 3.1. Electrochemical performance of positive electrode

Fig. 1 shows the discharge profiles of the harvested positive electrodes. The discharge capacities were 177.1 and 159.5 mAh g$^{-1}$ for the initial and cycled electrodes (70 °C), respectively. The values of capacity fading associated with the degradation were 10.0% for the sample cycled at 70 °C and 27.0% for that cycled at 80 °C [19]. As mentioned previously [19], most of the capacity fading of the entire cell cycled at 70 °C is attributed to that of the positive electrode.

Cyclic voltammograms of the positive electrodes after the initial conditioning and cycling at 70 °C are shown in Fig. 2. The cyclic curve for the fresh positive electrode exhibited three peaks on both the oxidation and reduction curves, corresponding to the phase transitions associated with the intercalation/deintercalation of Li ions [25]. The voltammogram of the positive electrode cycled at 70 °C, on the other hand, showed broader peaks than those of the fresh positive electrode, suggesting an increase in reaction resistance.

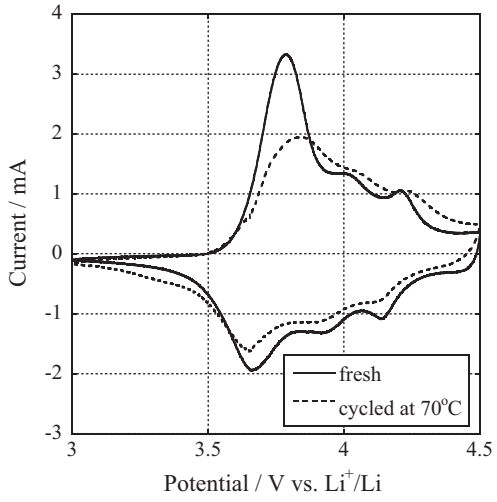


**Fig. 2.** Cyclic voltammograms obtained at 20 °C with scan rate of 0.2 mV s$^{-1}$ for positive electrodes of a fresh battery and one cycled at 70 °C.

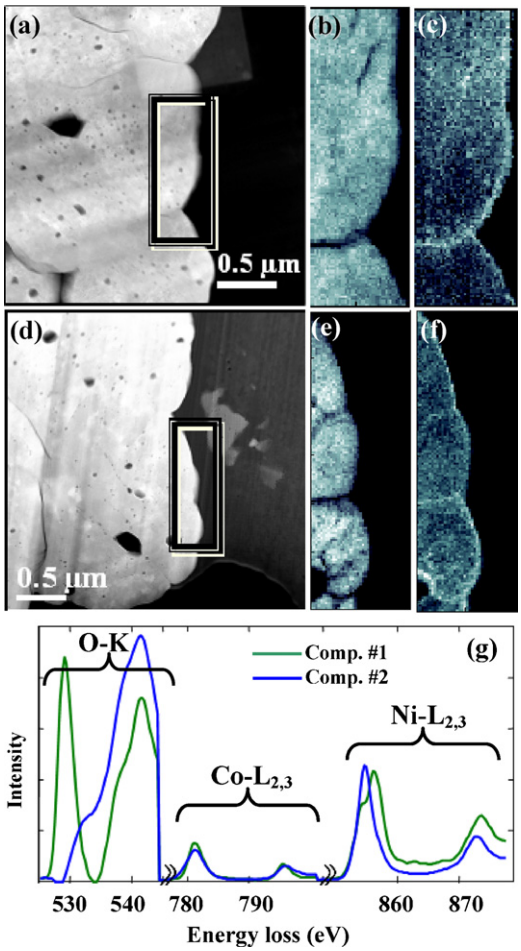


**Fig. 3.** Two-component MCR analysis of NCA cathode after initial conditioning (a–c) and after cycling at 70 °C (d–f): (a and d) ADF-STEM images of cathode. Framed areas were scanned for SI data acquisition. (b and e) Spatial distribution maps of component #1 (original phase). (c and f) Spatial distribution maps of component #2 (NiO-like phase). (g) Extracted spectral components.

Inductively coupled plasma-atomic emission spectroscopy (ICP-AES) was performed before the TEM sample preparation to confirm the lithium content in active materials. $x$ in $Li_xNi_{0.8}Co_{0.15}Al_{0.05}O_2$ was determined to be 0.99 and 0.87 for the fresh electrode and cycled electrode after discharging, respectively. The lithium content of the cycled electrode was never recovered to the initial lithium content even by discharging to 3.0 V vs. Li$^+$/Li, whereas almost all the lithium returned for the fresh electrode. It was implied that this irreversible lithium content was attributed to the capacity fading. We observed, however, no clear difference in crystal structure between the fresh and cycled positive electrode materials by conventional X-ray diffraction analysis although the lithium content was different from each other. It was hence considered that the degradation of the positive electrodes proceeded on the microscopic scale, undetected by macroscopic measurements.

### 3.2. Analysis of O–K, Co-$L_{2,3}$ and Ni-$L_{2,3}$ ELNESs

As has been shown previously [19,20], it is useful to examine the changes in the ELNESs of oxygen and transition metals to extract the spatial distributions and evolution of the assumed product phases. The STEM image and projected spatial distributions of the constituent phases resolved by the MCR analysis of the STEM-SI datasets are shown in Fig. 3a–c for the sample after

**Table 1**
Average radius of active material primary particles ⟨r⟩, average thickness ⟨Δz⟩ and its standard deviation σ, and volume fraction $\Delta VV^{-1}$ for NiO-like phase estimated from the experimental results for the respective samples. Cathode capacities electrochemically estimated for the samples are also listed for comparison.

| | Initial conditioning | 70 °C | 80 °C |
|---|---|---|---|
| <r> (nm) | 750 | 600 | 550 |
| ⟨Δz⟩ (nm) | 26 | 35 | 71 |
| σ (nm) | 9.8 | 20 | 47 |
| $1-\Delta VV^{-1}$ | 0.90(4) | 0.83(10) | 0.64(21) |
| $\Delta(\Delta VV^{-1})\times 100$ (%) | – | −8(10) | −24(15) |
| Cathode capacity (mAh g$^{-1}$) | 177.1 | 159.5 | 129.3 |
| Relative capacity change (%) | – | −10 | −27 |

the initial conditioning and in Fig. 3d–f for the sample after 500 cycles at 70 °C, where the number of constituent components was assumed to be two. Since the residual component exhibited an almost random spatial distribution pattern for both samples, it should be unnecessary to increase the number of components any more. The embedded spectral components resolved were found to be common for both samples, as shown in Fig. 3g. Comparing the spectral profiles of the resolved spectral components with those of the samples in the previous report (cycling at 80 °C), we found the lithium-deficient phase to be missing in the present study, which is not essential for the interpretation of the present results. The same primary product phase assigned to the NiO-like phase in the previous report is again distributed near the surface of primary active material particles in the present samples, as shown in Fig. 3c and f. The NiO-like phase seems to evolve after 500 cycles at 70 °C, but is less conspicuous than that observed in the sample cycled at 80 °C.

### 3.3. Quantitative estimation of NiO-like phase evolution

Since our group [19,20] and another group [12,14] have reported that the cathode degradation is mainly ascribable to the evolution of the NiO-like phase, it should be necessary to examine the quantitative correlation between capacity fading and the evolution of the NiO-like phase. The MCR analysis yields the normalized spectral profiles and their relative contributions to the entire experimental data set. If the ionization cross section of the corresponding core state is known, the contribution of each component can be converted to the relative concentration of the spectral component of interest. It was, however, found that the amount of NiO-like phase often tends to be overestimated because thin damage layers are formed on the sample surface during FIB thinning and that the O-K

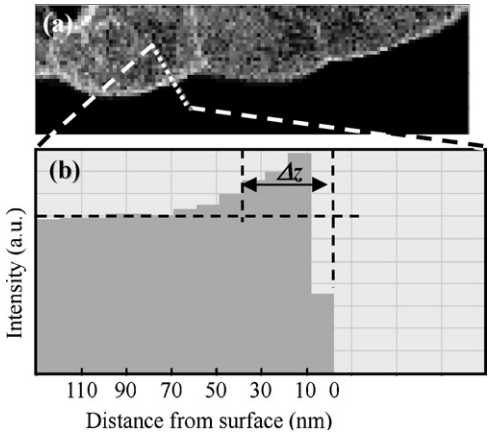


**Fig. 4.** (a) Typical example of spatial distribution map of NiO-like phase (reproduced from Fig. 1f). (b) Intensity distribution along white dotted line in (a). Δz is the estimated projected thickness of NiO-like phase.

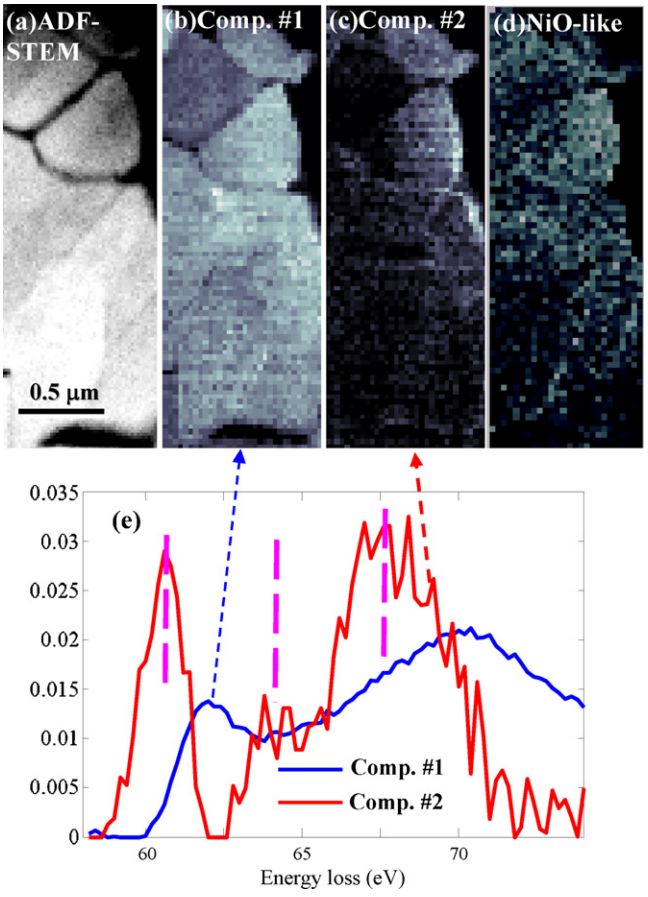


**Fig. 5.** Example results of Li analysis of the 70 °C cycled sample. (a) ADF-STEM image and (b) spatial distributions of component #1, (c) component #2 in MCR analysis in low-loss region and (d) NiO-like phase extracted from higher-energy spectral region for comparison. (e) Spectral components extracted by MCR analysis. Distinct peak positions are marked by pink broken lines. (For interpretation of the references to color in this figure legend, the reader is referred to the web version of the article.)

ELNES of the damage layer is very similar to that of the NiO-like phase.

Thus, to obtain a more robust estimation method, we measured the projected thickness of the NiO-like phase near surfaces or grain boundaries, because the NiO-like phase is likely to be localized around an active material particle surface in contact with the electrolyte, whereas the damage layer by FIB should uniformly cover the sample surface.

First, the intensity profile perpendicular to the surface or grain boundary was plotted at a selected area on an MCR map of the NiO-like phase, an example of which is shown in Fig. 4. The background baseline due to the surface damage layer was drawn along the constant intensity profile within the grain. The net thickness of the NiO-like phase was set equal to the distance between the surface and the half-maximum of the intensity profile of the inner-grain side, as shown in Fig. 4b. This procedure is justified because the formation of the NiO-like phase starts from the surface and proceeds gradually inward of the grain. Moreover, the thin degradation layer actually exhibits a steeper intensity profile, while the thick one shows a long intensity tail inward. The procedure was repeated for 40–50 profiles along the grain surfaces over the experimental data in each sample and the measured thickness values were statistically averaged. The obtained average thicknesses and their standard deviations of the NiO-like phase for the samples after the initial conditioning, cycled at 70 °C and 80 °C are listed in Table 1. The larger standard deviation for the more strongly degraded sample suggests that the degradation rate highly depends on grain

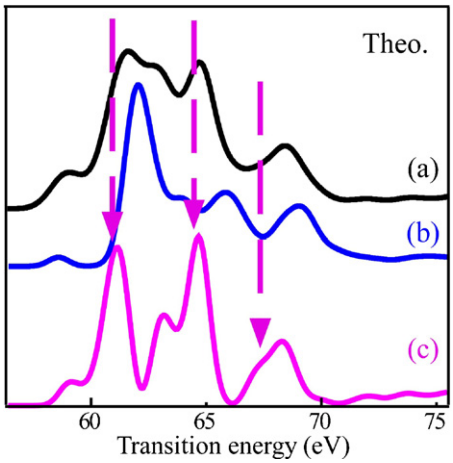


**Fig. 6.** Theoretical Li K ELNES assuming that Li is substituted at a Ni site in NiO (a), Li in $LiNiO_2$ (b) and difference spectra between the two (c). Pink broken lines correspond to those in Fig. 5e. (For interpretation of the references to color in this figure legend, the reader is referred to the web version of the article.)

morphology under different conditions, such as grain size, surface morphology and distance from the electrode surface.

To examine the correlation between the obtained amount of NiO-like phase and capacity fading, the following model was considered. For simplicity, the primary particle shape of the active material was assumed to be spherical. Then the size of many particles was measured for each type of sample. The radius of an irregular shape particle was calculated as the radius of the corresponding circle having the same projected area, and then the average radius of the particles was estimated. The average volume fraction of the NiO-like phase was deduced by calculating the ratio $4\pi \langle r\rangle^2 \langle \Delta z\rangle / 4/3\pi <r>^3$, where $<r>$ is the average particle radius and $\langle \Delta z\rangle$ is the estimated average NiO-like phase thickness. The derived volume fraction of the NiO-like phase in each sample is compared with the actual capacity fading in the last rows of Table 1. Since the number of grains measured was limited to ~10–20, the number of significant digits for the present estimation should be at most two. The relative capacity fading is quite consistent with the decrease in the volume fraction of the original phase. Considering the accuracies of the average particle radius, average NiO-like phase thickness and spherical particle assumption, it can be concluded that the present capacity fading is quite consistent with the amount of NiO-like phase evolved in the active material particles.

### 3.4. Analysis of Li–K ELNES

The SI data cubes extracted from the low-loss region covering the Li–K, Co-$M_{2,3}$ and Ni-$M_{2,3}$ edges were also treated by the MCR technique. The STEM image, spectral components extracted and their spatial distribution maps are, respectively, shown in Fig. 5a–c and e for the samples after 500 cycles at 70 °C as a result of 3-component analysis, in which the uniform background component was omitted. Component #1 (blue line (for interpretation of the references to color in this text, the reader is referred to the web version of the article)) corresponds to the original $LiNiO_2$-based phase, as shown in a previous study [21]. Component #2 (red line) in Fig. 5e is newly found in the cycled sample. This component is always found in the particles analyzed and its spatial distributions well correlate with those of the NiO-like phase at the same area, as shown in Fig. 5d for comparison. The present new phase and NiO-like phase are distributed near the surfaces in the particle grains, whereas lithium fluorophosphates are found in the initial state along the peripheries of the particle surfaces [21]. This suggests that component #2 could be interpreted to be lithium occupying the Ni site in the NiO structure. The point-to-point EELS analysis in our previous study [20] actually confirmed that lithium is present in the NiO-like phase.

The theoretical Li–K ELNES for substitution of a Li atom at a Ni site is shown in Fig. 6. Apparently, the theoretical ELNES does not well agree with the spectrum of component #2. However, the MCR procedure performed under certain conditions can yield a solution of the major component and a difference spectrum between the major and minor components, as shown in Appendix A. As has been mentioned in Ref. [21], for Li–K ELNES where transitions from shallow core states are studied, theoretical predictions based on the density functional theory (DFT) do not generally reproduce the experimental spectra well, particularly with respect to peak separation and relative peak intensities [21]. In spite of these

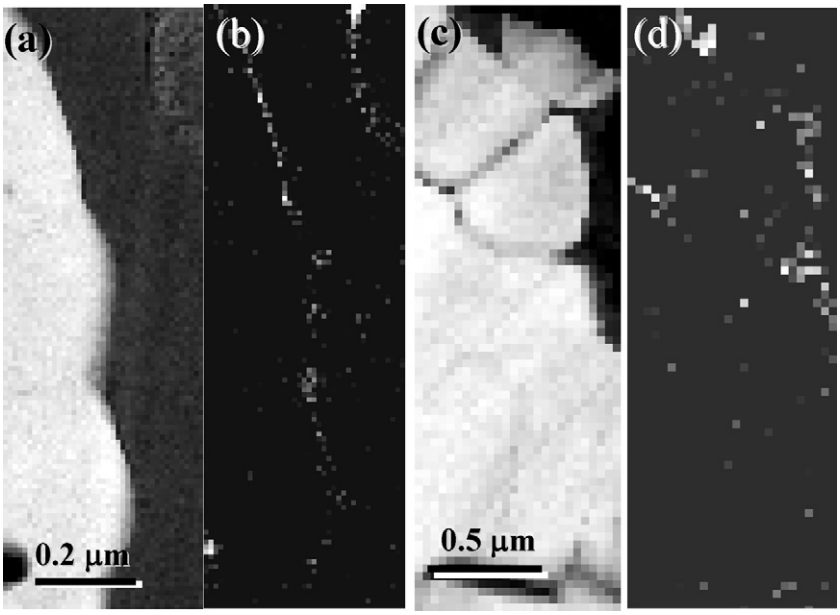


**Fig. 7.** Energy-filtered images selected for 695–705 eV with the pre-edge background subtracted, showing fluorine distributions in the same areas as those in Fig. 3d (after initial conditioning) and Fig. 5 (after 500 cycles at 70 °C).

difficulties, Fig. 6 actually shows that the theoretical difference spectrum between the Li–K spectra of $LiNiO_2$ and Li in NiO corresponds well to the MCR solution of component #2.

### 3.5. Fluorine distribution

The lithium fluorophosphates found along the particle surfaces and grain boundaries are not explicitly isolated by MCR in the cycled sample, partly because their main peak positions overlap with those of the Li–K ELNES in the NiO-like phase. To study the correlation between degradation and surface reaction with the electrolyte, the spatial distribution of fluorine was examined using energy-filtered images, as shown in Fig. 7, in which F-K-edge intensities are between the energy loss of 690 and 700 eV with the pre-edge background subtracted. Since the F-K ELNES intensities are nearly the same as the noise level, the ELNES was not clearly observed. The amount of fluoride after cycling at 70 °C seems to be decreased compared with that in the initially conditioned state. For the heavily degraded sample cycled at 80 °C, on the other hand, fluorine penetrated the areas where the NiO-like phase is distributed [21], so that we concluded that the surface reactions at the particle/electrolyte interface trigger oxygen evolution and the subsequent degradation. The present results at 70 °C suggest that surface fluorides have little to do with the NiO-like degraded phase formation.

## 4. Conclusions

We have shown using STEM–EELS and MCR that in NCA active material particles, the NiO-like phase grows near the surface and grain boundaries after 500 cycles at 70 °C, as observed in the same material cycled at 80 °C. We estimated the relative amounts of NiO-like phase before and after cycling at 70 and 80 °C, which mostly explained the capacity fading of the positive electrode. In accordance with the results above, it was shown that some Li atoms substitute for Ni atoms in the NiO-like degraded phase.

We can conclude from the results so far obtained that the degradation of NCA-type positive electrodes at elevated temperatures proceeds by evolution from an unstable $Ni_{1-x}(Co_x)O_2$ configuration locally formed by delithiation and the subsequent collapse of $NiO_6$ octahedra to the NiO-like phase. It is thus crucial to strengthen Ni–O bonds to suppress the degradation of the cathode, and Mg doping was proposed for such a purpose [25]. We theoretically considered the effects of Mg doping, based on the discussion on Mg-ELNES/XANES spectra [24], and the corresponding experimental evidence in terms of microstructures will be reported elsewhere.

## Acknowledgement

The present work is partly supported by a Grant-in-Aid for Scientific Research from MEXT, Japan (Priority Area #474, 'Atomic Scale Modification').

## Appendix A.

In this appendix, we will show using intuitive concepts and ideas rather than strict mathematical means that, under certain conditions, a minor component spectrum may be resolved into a major component and a difference spectrum between the minor and major component spectra. We adopt a two-component system to avoid unnecessary complication. Then an experimental dataset can be expressed in the form

$$X_i(E) = c_{i1}S_1(E) + c_{i2}S_2(E), \tag{A-1}$$

where $X_i(E)$ is the $i$th experimentally observed spectrum as a function of the energy loss $E$, $S_1(E)$ and $S_2(E)$ are pure component spectra and $c_{ij}$ is the relative fraction of each component in $X_i(E)$. In our case, each spectrum is normalized as

$$\int S_1(E)\,dE = 1, \quad \int S_2(E)\,dE = 1 \tag{A-2}$$

to relate $c_{ij}$ to the composition of each component spectrum. For simplicity, the Euclidian norm applies instead hereafter:

$$\int \left\|S_1(E)\right\|^2 dE = 1, \quad \int \left\|S_2(E)\right\|^2 dE = 1, \tag{A-2′}$$

where

$$\left\|S_1(E)\right\| = \sqrt{\sum_k s_{1k}^2}. \tag{A-3}$$

The summation in the square root stands for the sum of square of all the elements in $S_1(E)$, in which $k$ ranges over the channel number. This makes no essential difference in $S_1(E)$ and $S_2(E)$.

MCR may result in the following type of two-component resolution:

$$X_i(E) = (c_{i1} + b_{i1})S_1(E) + c_{i2}\left[S_2(E) - \frac{b_{i1}}{c_{i2}}S_1(E)\right], \tag{A-4}$$

where

$$b_{i1} \le c_{i2}, \quad \text{then} \quad \frac{b_{i1}}{c_{i2}} = q \le 1 \tag{A-5}$$

may in general hold because of the non-negativity constraint. Considering that the variable $E$ is actually discrete corresponding to the detector channel number, and each component spectrum is regarded as a vector in the $N$-dimensional space ($N$: number of channels in the detector), the MCR fitting converges into a solution so that the resolved component vectors make an angle as close to the right angle as possible. In the present case, $\boldsymbol{S}_1, \boldsymbol{S}_2$ and $\boldsymbol{S}_3$ are normalized and all the elements in those vectors are non-negative, and hence the angles $\theta_1$ between the vectors $\boldsymbol{S}_1$ and $\boldsymbol{S}_2$ can be defined as

$$\cos\theta_1 = S_1 \cdot S_2. \tag{A-6}$$

In this new MCR solution, the normalization should be in the form

$$\frac{\int \left\|S_2(E) - qS_1(E)\right\| dE}{a_{i2}} = \int \left\|S_3(E)\right\| dE = 1 \tag{A-7}$$

by introducing a new parameter $a_{i2}$, and Eqs. (A-4) and (A-7) yield

$$1 - q \le a_{i2} < \sqrt{1 + q^2}, \tag{A-8}$$

because $0 < \boldsymbol{S}_1 \cdot \boldsymbol{S}_2 \le 1$. Then Eq. (A-4) is rewritten as

$$X_i(E) = (c_{i1} + b_{i1})S_1(E) + c_{i2}a_{i2}S_3(E). \tag{A-9}$$

This new decomposition into $S_1$ and $S_3$ is possible so long as the minor component extends over the broader region than the major component in the energy-loss axis and Eq. (A-5) holds because of the non-negativity constraint.

The angle $\theta_2$ between $\boldsymbol{S}_1$ and $\boldsymbol{S}_3$ can then be written as

$$\cos\theta_2 = S_1 \cdot S_3 = S_1 \cdot \frac{S_2 - qS_1}{a_{i2}} = \frac{\cos\theta_1 - q}{a_{i2}},$$
$$< \frac{\cos\theta_1 - q}{1 - q} = \cos\theta_1 + \frac{\cos\theta_1 - 1}{1 - q}q < \cos\theta_1, \tag{A-10}$$

since $0 < q < 1$ and $\cos\theta_1 < 1$. It can be readily shown that $\theta_1$ and $\theta_2$ can be limited within the range from $-\pi/2$ to $\pi/2$ without losing the generality. Hence

$$\left|\theta_1\right| < \left|\theta_2\right|. \tag{A-11}$$

In this case, the difference spectrum $S_3(E)$, instead of the correct component spectrum $S_2(E)$, is thus preferably derived from the MCR treatment if the $S_2(E)$ extends over the broader range than $S_1(E)$, and Eq. (A-5) holds over the energy-loss range. These are the necessary conditions and this situation can occur when the minor component spectrum does not oscillate with large amplitudes and the spectral components $S_1(E)$ and $S_2(E)$ are not spatially isolated.

## References


[1] J.R. Dahn, U. von Sacken, C.A. Michal, Solid State Ionics 44 (1990) 87–97.
[2] J.R. Dahn, U. von Sacken, M.W. Juzkow, H. Al-Janaby, J. Electrochem. Soc. 138 (1991) 2207–2211.
[3] C. Delmas, I. Saadoune, Solid State Ionics 53–56 (1992) 370–375.
[4] E. Rossen, C.D.W. Jones, J.R. Dahn, Solid State Ionics 57 (1992) 311–318.
[5] T. Ohzuku, A. Ueda, M. Kouguchi, J. Electrochem. Soc. 142 (1995) 4033–4039.
[6] C. Delmas, M. Menetrier, L. Croguennec, I. Saadoune, A. Rougier, C. Pouillerie, G. Prado, M. Grune, L. Fournes, Electrochim. Acta 45 (1999) 243–253.
[7] C Pouillerie, L. Croguennec, Ph. Biensan, P. Willmann, C. Delmas, J. Electrochem. Soc. 147 (2000) 2061–2069.
[8] A. D'Epifanio, F. Croce, F. Ronci, V. Rossi Albertini, E. Traversa, B. Scrosati, Phys. Chem. Chem. Phys. 3 (2001) 4399–4403.
[9] S. Madhavi, G.V. Subba Rao, B.V.R. Chowdari, S.F.Y. Li, J. Power Sources 93 (2001) 156–162.
[10] X. Zhang, P.N. Ross Jr., R. Kostecki, F. Kong, S. Sloop, J.B. Kerr, K. Striebel, E.J. Cairns, F. McLarnon, J. Electrochem. Soc. 148 (2001) A463–A470.
[11] R. Kostecki, F. McLarnon, Electrochem. Solid-State Lett. 5 (2002) A164–A166.
[12] D.P. Abraham, R.D. Twesten, M. Balasubramanian, I. Petrov, J. McBreen, K. Amine, Electrochem. Commun. 4 (2002) 620–625.
[13] A.M. Andersson, D.P. Abraham, R. Haasch, S. MacLaren, J. Liu, K. Amine, J. Electrochem. Soc. 149 (2002) A1358–A1369.
[14] D.P. Abraham, R.D. Twesten, M. Balasubramanian, J. Kropf, D. Fischer, J. McBreen, I. Petrov, K. Amine, J. Electrochem. Soc. 150 (2003) A1450–A1456.
[15] A.M. Kannan, A. Manthiram, J. Electrochem. Soc. 150 (2003) A349–A353.
[16] J. Shim, R. Kostecki, T. Richardson, X. Song, K.A. Striebel, J. Power Sources 112 (2002) 222–230.
[17] C.H. Chen, J. Liu, M.E. Stoll, G. Henriksen, D.R. Vissers, K. Amine, J. Power Sources 128 (2004) 278–285.
[18] Y. Itou, Y. Ukyo, J. Power Sources 146 (2005) 39–44.
[19] T. Sasaki, T. Nonaka, H. Oka, C. Okuda, Y. Itou, Y. Kondo, Y. Takeuchi, Y. Ukyo, K. Tatsumi, S. Muto, J. Electrochem. Soc. 156 (2009) A289–A293.
[20] S. Muto, Y. Sasano, K. Tatsumi, T. Sasaki, K. Horibuchi, Y. Takeuchi, Y. Ukyo, J. Electrochem. Soc. 156 (2009) A371–A377.
[21] S. Muto, K. Tatsumi, T. Sasaki, H. Kondo, T. Ohsuna, K. Horibuchi, Y. Takeuchi, Electrochem. Solid-State Lett. 13 (2010) A115–A117.
[22] S. Muto, T. Yoshida, K. Tatsumi, Mater. Trans. 50 (2009) 964–969.
[23] P. Blaha, K. Schwarz, G.K.H. Madsen, D. Kvasnicka, J. Luitz, WIEN2k, an Augmented Plane Wave + Local Orbitals Program for Calculating Crystal Properties (Karlheinz Schwarz, Techn. Universität Wien, Austria), 2001. ISBN 3-9501031r-r1-2.
[24] K. Tatsumi, Y. Sasano, S. Muto, T. Yoshida, T. Sasaki, K. Horibuchi, Y. Takeuchi, Y. Ukyo, Phys. Rev. B 78 (2008) 045108.
[25] H. Kondo, Y. Takeuchi, T. Sasaki, S. Kawauchi, Y. Itou, O. Hiruta, C. Okuda, M. Yonemura, T. Kamiyama, Y. Ukyo, J. Power Sources 174 (2007) 1131–1136.